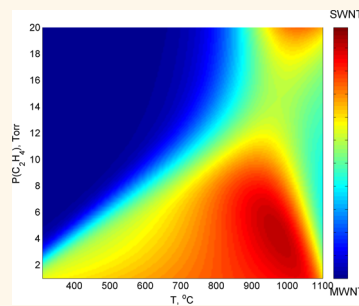


# Discovery of Wall-Selective Carbon Nanotube Growth Conditions *via* Automated Experimentation

Pavel Nikolaev,<sup>\*,†,‡</sup> Daylond Hooper,<sup>†,‡,§</sup> Nestor Perea-López,<sup>§</sup> Mauricio Terrones,<sup>§</sup> and Benji Maruyama<sup>†</sup>

<sup>†</sup>Air Force Research Laboratory, Materials and Manufacturing Directorate, RXAS, Wright-Patterson AFB, Ohio 45433, United States, <sup>‡</sup>UES Inc., Dayton, Ohio 45432, United States, and <sup>§</sup>Department of Physics, Pennsylvania State University, State College, Pennsylvania 16802, United States. <sup>§</sup>Present address (D.H.): Air Force Research Laboratory, RHCI, WPAFB, OH 45433 and Infoscitex Inc., Dayton, OH 45431, USA.

**ABSTRACT** Applications of carbon nanotubes continue to advance, with substantial progress in nanotube electronics, conductive wires, and transparent conductors to name a few. However, wider application remains impeded by a lack of control over production of nanotubes with the desired purity, perfection, chirality, and number of walls. This is partly due to the fact that growth experiments are time-consuming, taking about 1 day per run, thus making it challenging to adequately explore the many parameters involved in growth. We endeavored to speed up the research process by automating CVD growth experimentation. The adaptive rapid experimentation and *in situ* spectroscopy CVD system described in this contribution conducts over 100 experiments in a single day, with automated control and *in situ* Raman characterization. Linear regression modeling was used to map regions of selectivity toward single-wall and multiwall carbon nanotube growth in the complex parameter space of the water-assisted CVD synthesis. This development of the automated rapid serial experimentation is a significant progress toward an autonomous closed-loop learning system: a Robot Scientist.



**KEYWORDS:** carbon nanotube synthesis • automatic • selectivity

Carbon nanotubes have an unprecedented combination of mechanical, electrical, thermal, and electronic properties that make them available for applications ranging from structures to devices to sensors to name but a few. However, despite decades of research, the synthesis of carbon nanotubes (CNTs) is not sufficiently well-controlled to fulfill their promise. The lack of control persists despite attempts at empirical optimization and thus leads us to focus on extending the fundamental understanding of CNT growth. An important barrier to our fundamental understanding is the very large expanse of experimental parameters that define a chemical vapor deposition (CVD) growth experiment (such as temperature, gas flow rates, compositions, concentrations, etc.). The slow rate at which growth experiments are conducted (~1 per day) combines with the large experimental parameter space to overwhelm our ability to explore it, thereby impeding the progress of understanding and improving growth. To this end, we have developed the first system to automate the

exploration of parameter space for carbon nanotube growth, which we use to understand and control selective growth of single-wall and multiwall carbon nanotubes.

The evolution of carbon nanotubes dates back to carbon nanofibers (CNFs), which were first grown by CVD as far back as 1952,<sup>1</sup> followed by broader acceptance of the CVD technique for the synthesis of CNFs and what was later recognized as multiwall nanotubes (MWNTs) in the 1970s.<sup>2–4</sup> Single-wall carbon nanotubes (SWNTs), found in the products of carbon arc discharge by Iijima<sup>5</sup> and Bethune,<sup>6</sup> turned out to be more difficult to produce by CVD, even though they probably existed in Endo's CVD products.<sup>4</sup> Dai *et al.*<sup>7</sup> were the first to demonstrate SWNT growth from carbon monoxide in 1996, quickly followed by SWNT syntheses from more common hydrocarbon feedstocks in 1998.<sup>8–10</sup> The SWNT yields and production rates, however, remained rather low (with the exception of the HiPco process).<sup>11</sup>

An important breakthrough came in 2004, when Hata *et al.* reported water-assisted

\* Address correspondence to pavel.nikolaev.ctr@us.af.mil.

Received for review June 19, 2014 and accepted October 9, 2014.

Published online October 09, 2014  
10.1021/nn503347a

© 2014 American Chemical Society

synthesis ("supergrowth") of SWNTs by ethylene CVD.<sup>12</sup> It was shown that 175 ppm of water vapor in the CVD feedstock was a magic ingredient that allowed growing few millimeter high SWNT carpets by greatly extending the catalyst lifetime, while achieving exceptionally high growth rates, on the order of 2–10  $\mu\text{m/s}$ .<sup>13</sup> Since then, water has been widely used as a promoter in CNT growth. Selectivity toward SWNTs (or any other kind of CNT), however, remains problematic. While the first publication demonstrated SWNT growth,<sup>12</sup> double-wall nanotubes (DWNTs) or MWNTs were also present. Selectivity toward DWNTs was demonstrated soon,<sup>14–16</sup> with small quantities of SWNTs and MWNTs observed, as well as selectivity toward MWNTs.<sup>17</sup> A number of publications explain strategies for wall selectivity. The nanotube diameter and average number of walls were shown to be proportional to the catalyst thickness (and therefore catalyst particle size).<sup>15,16,18–20</sup> Even with a fixed catalyst thickness, changes in the temperature<sup>21,22</sup> and feedstock pressure<sup>21–23</sup> also affect the number of walls nucleated. All of these publications have shown that a typical product is still a mixture of nanotube types with varying ratios of SWNTs, DWNTs, and MWNTs—that is, not selective.

Puretzky *et al.*<sup>21,22</sup> provided an interesting insight into the mechanism that determines the number of CNT walls (hereafter referred to as the Puretzky model): The authors argue that the number of CNT walls is determined by the interplay between the incident carbon flux and the ability of a single growing cylinder (SWNT) to accept incoming C atoms. They postulate that when the carbon supply outpaces the rate at which carbon atoms can be added to a SWNT, an additional wall is nucleated. For a given flux, SWNTs will grow at elevated temperature due to faster carbon atom addition kinetics, but MWNTs will grow at lower temperature due to the inability of a SWNT to accommodate the incoming flux of carbon atoms. The cross-over temperature is defined as the temperature at which growth transitions from SWNTs to MWNTs. Increasing the partial pressure of the hydrocarbon leads to an increase in the incoming carbon flux and shifts SWNT/MWNT crossover temperature higher, which is consistent with later observations.<sup>23</sup> We note that the Puretzky model is deterministic in nature; that is, it predicts the number of CNT walls but does not account for typically observed stochastic CNT-type mixtures. The diversity of CNT types within an individual experiment strongly suggests that nanotube nucleation is probabilistic in nature; that is, there are certain probabilities of nucleating SWNTs or MWNTs at a given CVD condition, and thus selectivity toward certain product is achieved by maximizing the respective probability, while minimizing other ones.

The adaptive rapid experimentation and *in situ* spectroscopy (ARES) system continues to be developed by us in our effort to more effectively explore and

understand nanotube growth. Previously, we demonstrated the value of *in situ* spectroscopy by tracking the growth rate of a carbon nanotube and showing that the growth rate increased with chiral angle.<sup>24</sup> We also showed that the lifetime of a catalyst and the nucleation success rate correlated to the liquid or solid state of the catalyst.<sup>25</sup> Due to the stochastic nature of nanotube growth, this phenomenon only became clear because of the large number (>100) of experiments enabled by ARES. In our current effort, we begin to address the problem of the large parameter space of input conditions for CVD growth. Input parameters for a CVD growth experiment include the following: temperature, pressure, choice of hydrocarbon, concentrations and flow rates of hydrogen, water vapor, inert gases, and carbon source; choice of catalyst, catalyst support, catalyst promoters, calcination conditions, and reduction conditions are all important. Additionally, the range of many parameters is large: growth temperature can vary from 400 to 1500 °C and pressures from  $10^{-5}$  to tens of atmospheres (>6 orders of magnitude). There is also a large number of pure elemental catalysts<sup>26</sup> and perhaps an exponentially large number of choices when binary, ternary, and more complex catalysts are considered.

Facing such an overwhelming number of potential growth conditions to explore, it is imperative that the rate of experimentation be increased *via* automation. Previous work in automated experimentation includes workstation for automated nanomaterial discovery and analysis (WANDA),<sup>27</sup> developed for automated nanocrystal synthesis. WANDA's liquid-handling robotics inject precursor chemicals into an array of reactors, followed by rapid screening of the structural and optical properties of resulting nanocrystals, also using automated methods. Automation of the synthesis and analysis allows WANDA to optimize the size, crystal structure, and luminescence properties of nanocrystals. Another example is Adam,<sup>28,29</sup> designed to study functional yeast genomics. Three robotic arms combine planned yeast strains, metabolites, and growth medium, followed by automatic optical density measurements that act as a proxy for cellular growth. Biologically significant parameters were extracted from the optical data and statistically analyzed to update the model of yeast metabolism. Adam was successfully used to identify genes responsible for catalyzing specific reactions in the metabolic pathways of the yeast *Saccharomyces cerevisiae*<sup>28</sup> and for the rapid screening of antiparasitic drugs.<sup>30</sup> An excellent review<sup>29</sup> makes it clear that, at present, experimental systems stemming from life sciences are considered most amenable to automation of experimentation. For carbon nanotube synthesis, there are a number of reports utilizing combinatorial approaches to study catalyst libraries for CNT growth.<sup>31–33</sup> This kind of massively parallel approach has a certain limitation:

while catalyst composition is varied, the CVD growth conditions are the same across the library, and the analysis remains unautomated, is labor-intensive, and is still mostly done in a serial fashion.

The only example of high-throughput CNT synthesis is from Hart *et al.*,<sup>46</sup> who demonstrated automated synthesis using Robofurnace. Their work elucidated the variability in experimental outcomes despite efforts to precisely control growth conditions. They used *in situ* video capture to monitor CNT forest height during growth; however, they did not capture information on the CNT type.

Our ARES system was developed with the target milestone of increasing the rate of experimentation by 100-fold, to 100 runs per day, with results analyzed *in situ* and in real time *via* Raman spectroscopy. We have achieved this goal. Additionally, the system is now capable of running a 25-experiment series in fully automatic mode, with preprogrammed growth recipes and without user intervention, as opposed to previously published results<sup>24,25</sup> when each experiment was done in an essentially manual fashion. This approach is distinct from combinatorial approaches mentioned above because the experiments are done in rapid serial fashion, rather than parallel, and thus the growth recipe can be varied for each experiment.

## RESULTS

Below we discuss the selectivity of the water-assisted CVD toward SWNT or MWNT nucleation. The CNT growth kinetics determined from the time dependence of the G- and D-band intensity will be the subject of a follow-up article.

A data set of 534 growth experiments was produced for this article. The temperature was varied from 400 to 1100 °C, pressure from 4 to 40 Torr, and water concentration from 4 to 280 ppm. The type of nanotube (*i.e.*, single-wall or multiwall) was determined from characteristic features of the Raman G- and D-bands. Typical nanotube spectra are shown in Figure 1. SWNT spectra (Figure 1a) are characterized by a narrow G-band and almost absent D-band. MWNT spectra (Figure 1b) are characterized by broad D- and G-bands of about equal intensity. Often both MWNT and SWNT growth is detected (referred to as “mixed growth”), with spectra being essentially a superposition of MWNT and SWNT features, that is, a narrow SWNT G-band atop a broad MWNT G-band (Figure 1c). These spectral characteristics were used to assign binary growth type identifiers:

- [10] = SWNT
- [01] = MWNT
- [11] = SWNT and MWNT
- [00] = no growth

The results of 129 experiments were additionally characterized by SEM imaging and *ex situ* Raman

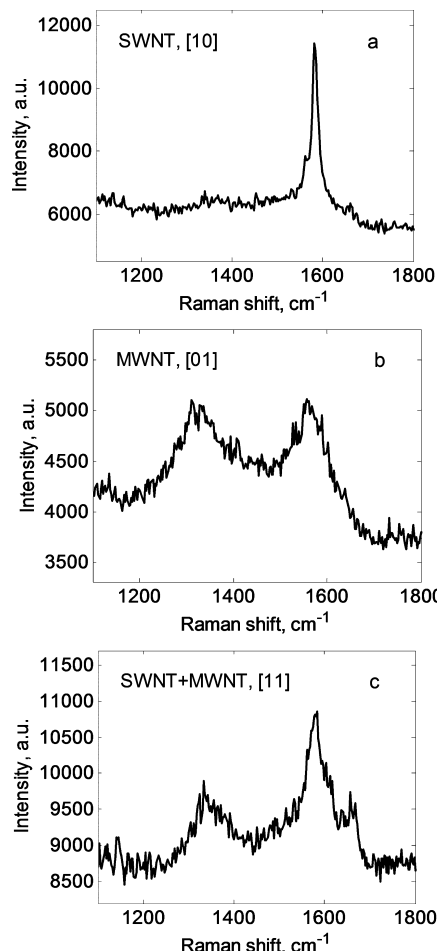
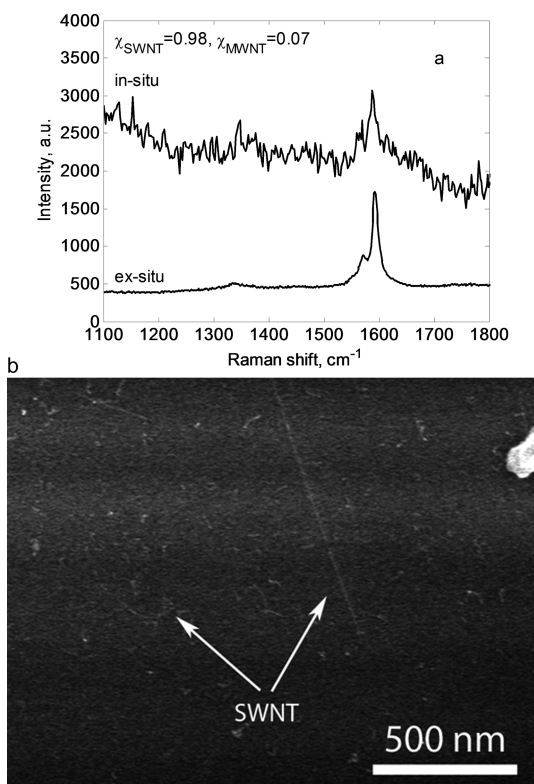


Figure 1. Examples of Raman spectra obtained *in situ* on SWNT (a), MWNT (b), and SWNT+MWNT (c) (mixed growth).

spectroscopy in a commercial spectrometer to confirm the *in situ* identification, and seven of those (5.4%) had to be corrected. Misidentification was caused by lower signal-to-noise ratio of the *in situ* spectra when nanotube growth was weak, and the better light collection efficiency and longer exposures afforded in the commercial Raman system provided more reliable identification in these cases. An example of a correct *in situ* identification confirmed by *ex situ* analysis is shown in Figure 2. An example of the incorrect *in situ* identification that had to be corrected after *ex situ* analysis is shown in Figure 3.

The results were analyzed using logical regression.<sup>35</sup> Logical regression is a technique developed to analyze correlations within data sets containing a mix of continuous and discrete variables. This is appropriate because experimental outcome of single-wall or multiwall growth is discrete, whereas experimental inputs (*e.g.*, temperature or pressure) are continuous. The probabilities of growing SWNTs ( $\chi_{\text{SWNT}}$ ) and MWNTs ( $\chi_{\text{MWNT}}$ ) were assumed to be independent in order to allow for mixed growth; therefore, two separate models were constructed for  $\chi_{\text{SWNT}}$  and  $\chi_{\text{MWNT}}$ . The predictor variable matrix was constructed from



**Figure 2.** Example of correct *in situ* identification. *In situ* and *ex situ* Raman spectra (a) and SEM image (b) showing several SWNTs. The experiment was identified as [10] (SWNT only).

experimental inputs: partial pressures of the constituent gases  $P(C_2H_4, \text{ Torr})$  and  $P(H_2, \text{ Torr})$ , water concentration (ppm), and temperature  $T$  (°C) for each experiment (eqs 2 and 3). The response vector  $p_{\text{SWNT}}$  for the SWNT model comprised a binomial variable which was set to 1 when either SWNT or mixed growth was detected ([10] or [11]) and 0 when no SWNT was detected ([01] or [00]) (eq 2). Likewise, the binomial response vector  $p_{\text{MWNT}}$  for the MWNT model was set to 1 when either MWNT or mixed growth was detected ([01] or [11]) and 0 when no MWNT was detected ([10] or [00]) (eq 3). Therefore, the first model output was the probability of growing the SWNT,  $\chi_{\text{SWNT}}$ , regardless of whether a MWNT grew or did not grow, and the second model output was  $\chi_{\text{MWNT}}$ . The 129 experiments that were additionally analyzed *ex situ* by SEM/Raman were weighed two times higher than the rest of the experiments. It has to be noted that the terms and coefficients of the resulting polynomials do not themselves bear physical meaning, being simply a result of mapping of probabilities using second degree polynomials. The resulting dependencies, however, express correlations between the input parameters and the probability of the outcomes.

Visualization of the output of regression models presents certain difficulties since the parameter space is four-dimensional. Two-dimensional slices through the four-dimensional parameter space of the SWNT and MWNT models are shown in Figure 4. Probabilities

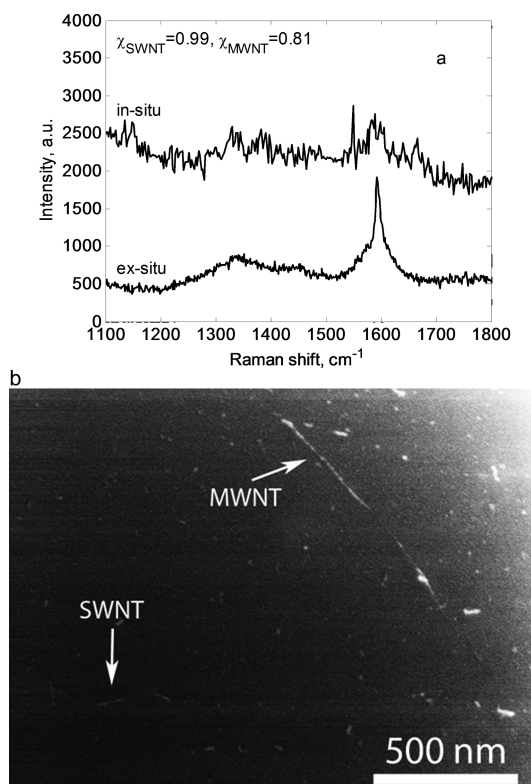


**Figure 3.** Example of corrected *in situ* identification. The experiment was misidentified as [01] (MWNT only) based on noisy *in situ* spectrum (a) and corrected to [11] (SWNT+MWNT) based on *ex situ* spectrum (a) and SEM imaging (b) showing both SWNTs and MWNTs present on the pillar.

of nucleating SWNTs (Figure 4a) and MWNTs (Figure 4b) are plotted with respect to the temperature and  $C_2H_4$  partial pressure, with other inputs fixed at typical average values:  $P(H_2) = 12$  Torr and  $H_2O = 50$  ppm. It can be seen that  $\chi_{\text{SWNT}}$  has a well expressed maximum at low  $C_2H_4$  partial pressures, in the  $\sim 700$ – $900$  °C temperature range.  $\chi_{\text{MWNT}}$ , on the other hand, is maximized in the upper range of the  $C_2H_4$  partial pressure and at  $T < 600$  °C. These results agree well with our observations: MWNTs tend to grow at high  $C_2H_4$  partial pressure and low temperature, and SWNTs tend to grow at high temperature and low  $C_2H_4$  pressure.

The results presented in Figure 4 are the outputs of the regression model. For a comparison to the experimental results, see Supporting Information Figure S2.

Figure 4 shows the probability of growing either CNT type regardless of whether another CNT type grows, as well. Selective growth of SWNTs or MWNTs, however, should be defined as the region in the parameter space where the probability of nucleating either CNT type is maximized, whereas another CNT type is minimized; that is, the binary growth type identifiers are [10] and [01] for the selective SWNT and MWNT nucleation. The respective probabilities,  $\chi_{\text{SWNT ONLY}}$  and  $\chi_{\text{MWNT ONLY}}$  are plotted in Figure 5a,b, respectively. It can be seen that the region of selectivity toward SWNTs is located

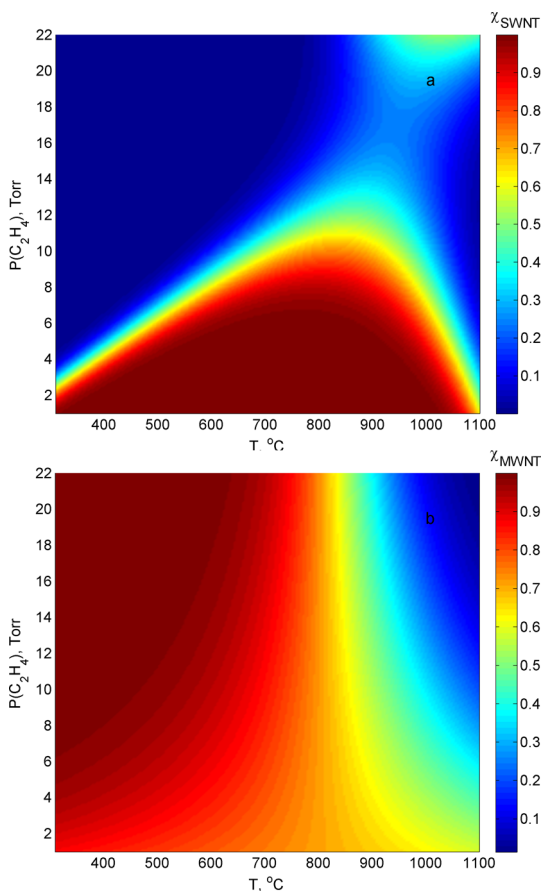


**Figure 4.** Probabilities of nucleating SWNTs (a) and MWNTs (b) with respect to temperature and  $\text{C}_2\text{H}_4$  partial pressure, with other inputs fixed at typical average values:  $P(\text{H}_2) = 12$  Torr and  $\text{H}_2\text{O} = 50$  ppm.

at  $T = \sim 975^{\circ}\text{C}$  and  $P(\text{C}_2\text{H}_4) = 5$  Torr, while the region of selectivity toward MWNTs is in a broader region where  $T < \sim 600^{\circ}\text{C}$  and  $P(\text{C}_2\text{H}_4) > \sim 8$  Torr (with other inputs fixed at typical average values:  $P(\text{H}_2) = 12$  Torr and  $\text{H}_2\text{O} = 50$  ppm). Because the maxima are extrapolations just beyond the range of experimental data (Figure S2), they should be viewed as general regions of interest rather than precise values. It is also important to note that the probability of growing either SWNTs or MWNTs is never zero in the regions where probability of growing MWNTs or SWNTs is maximized. Therefore, a “perfect” selectivity does not exist: the typical product is a mixture of CNT types, in agreement with the results observed in the literature.<sup>12,14–16,18–20</sup> It should be possible, however, to maximize the SWNT or MWNT fraction to a rather high extent.

The observed tendency of SWNTs to grow at low  $\text{C}_2\text{H}_4$  partial pressure and high temperature, and MWNTs at high  $\text{C}_2\text{H}_4$  pressure and low temperature, is in a good agreement with the Puretzky model,<sup>22</sup> in which an increase in the hydrocarbon partial pressure shifts the SWNT/MWNT crossover temperature up. The probabilities of nucleating SWNTs and MWNTs with respect to temperature for two values of  $\text{C}_2\text{H}_4$  partial pressure are plotted in Figure 6. For any given

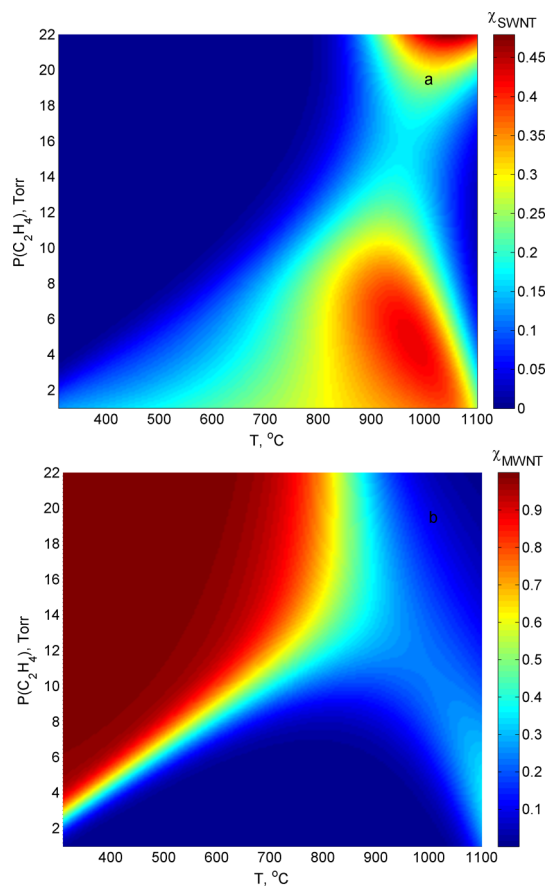


**Figure 5.** Probabilities of selective nucleation of SWNTs (a) and MWNTs (b) with respect to temperature and  $\text{C}_2\text{H}_4$  partial pressure, with other inputs fixed at typical average values:  $P(\text{H}_2) = 12$  Torr and  $\text{H}_2\text{O} = 50$  ppm.

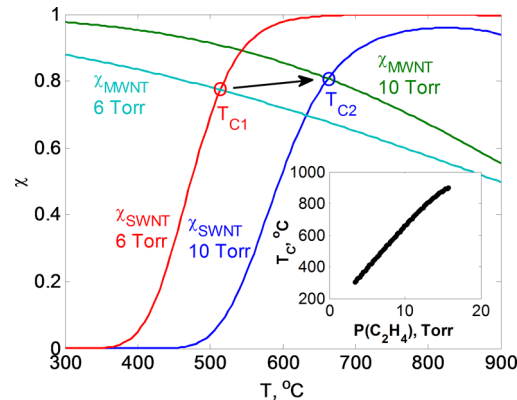


**Figure 6.** Probabilities of nucleating SWNTs and MWNTs with respect to temperature for 6 and 10 Torr  $\text{C}_2\text{H}_4$  partial pressure, with other inputs fixed at typical average values:  $P(\text{H}_2) = 12$  Torr and  $\text{H}_2\text{O} = 50$  ppm. Crossover temperatures (above which  $\chi_{\text{SWNT}} > \chi_{\text{MWNT}}$ ) are marked with a red circle ( $T_{\text{C}1}$ , 6 Torr) and blue circle ( $T_{\text{C}2}$ , 10 Torr>).  $T_{\text{C}}$  dependence on the  $\text{C}_2\text{H}_4$  partial pressure is shown in the inset.

temperature, increase in the hydrocarbon pressure leads to lower  $\chi_{\text{SWNT}}$  and higher  $\chi_{\text{MWNT}}$ , which shifts overall SWNT/MWNT balance toward MWNTs. Similarly, for any given hydrocarbon pressure, an increase in the temperature leads to higher  $\chi_{\text{SWNT}}$  and lower

$\chi_{\text{MWNT}}$ , shifting the SWNT/MWNT balance toward the SWNT. Since regression analysis is probabilistic, we can redefine the crossover temperature  $T_C$  as the one where  $\chi_{\text{SWNT}} = \chi_{\text{MWNT}}$ , that is,  $\chi_{\text{SWNT}} > \chi_{\text{MWNT}}$  when  $T > T_C$ . Crossover temperatures are marked in Figure 6 with a red circle (6 Torr  $\text{C}_2\text{H}_4$ ) and blue circle (10 Torr  $\text{C}_2\text{H}_4$ ), and  $T_C$  dependence on the  $\text{C}_2\text{H}_4$  partial pressure is shown in the inset. It can be seen that an increase in the hydrocarbon pressure shifts  $T_C$  up, according to the upward trend discussed above.

This brings us to the role of water in the “super-growth”. It has been accepted that a small amount of water in the CVD reactor acts as a weak oxidizer and selectively removes amorphous carbon without damaging the growing CNTs.<sup>12</sup> A different, although not mutually exclusive, idea of the role of water also emerged:<sup>36,37</sup> that water creates  $-\text{OH}$  groups on the alumina catalyst support, thus impeding catalyst particle mass loss *via* Ostwald ripening, which otherwise leads to the disappearance of small particles necessary to support SWNT growth. This idea is supported by earlier observations<sup>38</sup> that very fast heating maximizes CNT growth, which in retrospect may be due to most of the growth occurring before Ostwald ripening takes place. There also is some agreement that too much water leads to growth suppression *via* catalyst oxidation<sup>13,39</sup> and damage to nanotubes.<sup>20</sup>

Probabilities of nucleating SWNTs and MWNTs with respect to temperature and  $\text{H}_2\text{O}$  concentration with other inputs fixed at typical average values,  $P(\text{H}_2) = 12$  Torr and  $P(\text{C}_2\text{H}_4) = 8$  Torr, are shown in Figure 7. For a comparison to the experimental results, see Supporting Information Figure S3. It can be seen that  $\chi_{\text{SWNT}}$  is maximized in the 700–900 °C temperature range and above  $\sim 100$  ppm of  $\text{H}_2\text{O}$  concentration.  $\chi_{\text{MWNT}}$ , on the other hand, is maximized at  $T < \sim 600$  °C and  $\text{H}_2\text{O}$  concentration less than  $\sim 100$  ppm.  $\chi_{\text{SWNT}}$  increases as the water concentration goes up and does not exhibit a maximum below 280 ppm of  $\text{H}_2\text{O}$ , the upper range of the water concentration in the experimental set. This result is in good agreement with the idea that water prevents loss of small catalyst particles *via* Ostwald ripening.<sup>36,37</sup> Indeed, it appears that MWNTs nucleate preferentially below  $\sim 100$  ppm concentration, while SWNT nucleation is suppressed, indicating that there's not enough water to prevent Ostwald ripening. On the other hand, SWNTs nucleate preferentially above  $\sim 100$  ppm, indicating that there is enough water to prevent Ostwald ripening, and small particles remain small and promote SWNT nucleation. This argument assumes that nanotube diameter is commensurate with the catalyst particle size.<sup>15,16,18–20</sup>

The influence of the water content on the type of CNT can be seen further in Figure 8, which shows  $T_C$  dependence on the  $\text{C}_2\text{H}_4$  partial pressure for several water concentrations. An increase in the water concentration at the same  $\text{C}_2\text{H}_4$  partial pressure shifts the

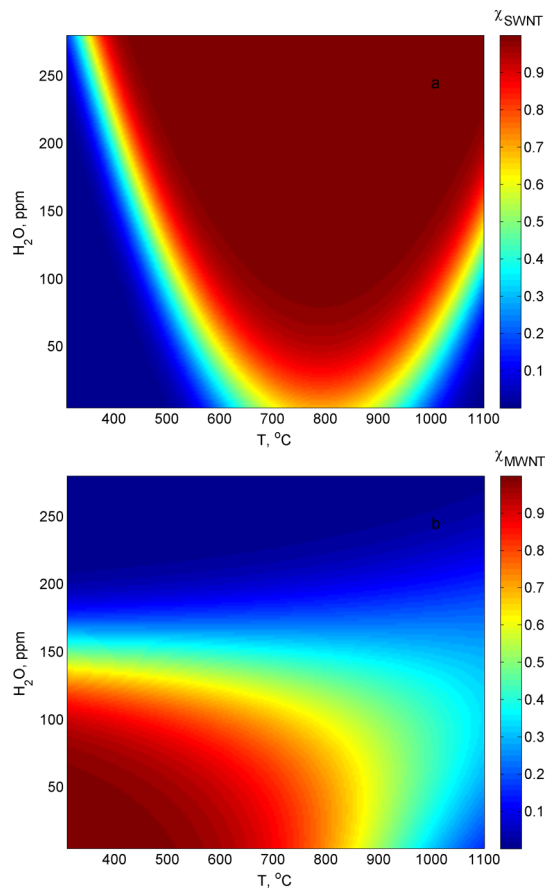


Figure 7. Probability of nucleating SWNTs (a) and MWNTs (b) with respect to temperature and  $\text{H}_2\text{O}$  concentration, with other inputs fixed at typical average values:  $P(\text{H}_2) = 12$  Torr and  $P(\text{C}_2\text{H}_4) = 8$  Torr.

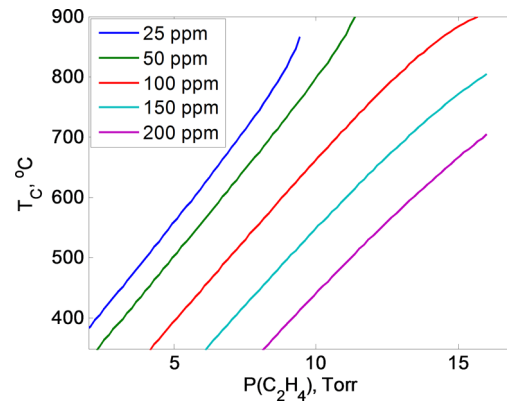


Figure 8. Crossover temperature  $T_C$  dependence on the  $\text{C}_2\text{H}_4$  partial pressure for several values of  $\text{H}_2\text{O}$  concentration.

crossover temperature down; that is, the probability of nucleating the SWNT goes up. Therefore, an increase in the  $\text{H}_2\text{O}$  concentration has the same effect on the SWNT/MWNT balance as does a decrease in the hydrocarbon pressure. This observation points toward the water role in the CVD chemistry: it reacts with the carbon precipitating on the catalyst particle and removes it in the form of volatile oxides ( $\text{CO}$ ,  $\text{CO}_2$ ), effectively reducing the incoming carbon flux.<sup>12</sup>

## CONCLUSIONS

We were able to map regions of selectivity toward SWNT and MWNT nucleation and growth in four-dimensional parameter space of the water-assisted CVD synthesis using a statistical linear regression analysis of 534 growth experiments, analyzed by Raman spectroscopy, mostly *in situ*. This is the first demonstration of automated experimentation combined with regression analysis applied to understanding CNT synthesis. We built the ARES system to address the problem of an overwhelmingly large experimental parameter space, as well as the slow experimentation rate and statistical variability in experimental outcomes. We found that the large quantity of experimental results enabled by automation were best treated using logical regression.

The results of the regression analysis are in a good agreement with the Puretzky model<sup>22</sup> in terms of the shift of the SWNT/MWNT boundary with respect to temperature and hydrocarbon pressure. The role of the water agrees with its effect on the size of catalyst particles *via* Ostwald ripening<sup>36,37</sup> and with its ability to “mop up” extra carbon from the catalyst.<sup>12</sup> The predictive power of the regression analysis is further emphasized using examples presented in Figures 2 and 3: probabilities of SWNT and MWNT nucleation are  $\chi_{\text{SWNT}} = 0.98$  and  $\chi_{\text{MWNT}} = 0.07$  in the SWNT case (Figure 2) and  $\chi_{\text{SWNT}} = 0.99$  and  $\chi_{\text{MWNT}} = 0.81$  in the case of mixed growth (Figure 3); that is, the prediction is in excellent agreement with the experiment.

An additional benefit of the regression analysis is that it can be done on a limited number of experimental results and can then guide future experimentation, helping to define regions of interest in the

four-dimensional parameter space. An attempt to cover the parameter space with experiments uniformly is intractable: for example, a grid of only 10 values of each parameter yields  $10^4$  experiments, which is prohibitive even for ARES. In this particular set of experiments, early analysis helped to direct our efforts toward higher water concentrations, where SWNTs nucleate preferentially, and to experiment with higher fidelity in the regions where  $\chi_{\text{SWNT}}$  and  $\chi_{\text{MWNT}}$  are maximized: high temperature/low hydrocarbon pressure and low temperature/high hydrocarbon pressure, respectively. The regression analysis presented here was done manually and off-line. When similar analysis is done after *each* experiment, automatically and in real time, it could guide the design of subsequent experiments, closing the experimentation loop. This approach will let the machine design and execute its own experiments based on a certain goal such as selectivity, growth rate, etc.

Regression analysis is only one of many tools being developed and deployed on ARES to close the experimental loop. These include the use of other statistical approaches, computational optimization, and artificial intelligence-based solutions, to include neural networks, support vector machine,<sup>40</sup> random forests,<sup>41</sup> genetic algorithms, and optimal learning with knowledge gradient approach.<sup>42</sup> Advantages of these techniques are an ability to determine complex relationships between many input parameters to provide a robust consensus view<sup>43</sup> of nanotube growth and determine input parameters with the largest effect on results. This contribution is a major milestone in the larger effort to accelerate materials discovery through the autonomous experimentation.

## EXPERIMENTAL SECTION

The ARES instrument diagram is shown in Figure S1, Supporting Information. CNTs are grown in a cold-wall CVD chamber installed on a three-axis motion stage above an inverted Raman microscope (Nikon Ti-E). The growth substrate consists of  $5 \times 5$  arrays of silicon pillars spaced  $50 \mu\text{m}$  apart on a  $\text{SiO}_2$  sublayer,  $10 \mu\text{m}$  tall and  $10 \mu\text{m}$  diameter (Figure S1 inset). Pillars are coated with  $10 \text{ nm}$  ALD alumina support layer and  $1 \text{ nm}$  Ni catalyst film deposited by ion beam sputtering. Each pillar constitutes essentially an independently addressable microreactor, which is heated by a  $532 \text{ nm}$  laser beam that doubles as a Raman excitation source through a  $50 \times$  extra-long working distance objective lens. Raman spectra are collected from a  $\sim 5 \mu\text{m}$  size spot illuminated by the excitation laser. The small thermal mass of the pillar combined with low thermal conductivity of the  $\text{SiO}_2$  sublayer enables heating to reaction temperatures within a fraction of a second when laser power is varied in the  $0\text{--}1.5 \text{ W}$  range. CVD chamber pressure is measured by a capacitance pressure gauge (MKS) and regulated by a throttle valve (MKS) exhausting into a vacuum pump.  $\text{H}_2$ ,  $\text{C}_2\text{H}_4$ , and  $\text{Ar}$  feedstock gases are metered into the CVD chamber in varying ratios *via* mass flow controllers (MKS). Water vapor is bled into the chamber through a manual leak valve, and its concentration is measured by a dew point sensor (Shaw). The temperature-induced shift of the Si Stokes and anti-Stokes Raman bands

( $\pm 520 \text{ cm}^{-1}$ ) is used to calculate the growth temperature according to eq 1:

$$\Delta\omega(T) = C \left[ 1 + \frac{2}{\frac{\hbar\omega_0}{e^{2k_B T} - 1}} \right] + D \left[ 1 + \frac{3}{\frac{\hbar\omega_0}{e^{3k_B T} - 1}} + \frac{3}{\left( \frac{\hbar\omega_0}{e^{3k_B T} - 1} \right)^2} \right] \quad (1)$$

Here  $k_B$  is Boltzmann's constant,  $\hbar$  is Planck's constant, and  $\omega_0$ ,  $C$ , and  $D$  are constants with the values  $528$ ,  $-2.96$ , and  $-174 \text{ cm}^{-1}$ , respectively.<sup>34</sup> The accuracy of the temperature measurement is estimated to be within  $\sim 10\text{--}15 \text{ }^\circ\text{C}$ .

The  $x\text{-}y\text{-}z$  stage, mass flow controllers, pressure controller, microscope, laser, and spectrometer are all simultaneously controlled by custom software developed for 64-bit Windows 7 in C#/Net 4.0 using Windows Visual Studio 2010. Abstraction and object-oriented programming are incorporated into the software design in order to take advantage of concurrencies in the hardware. In a series of experiments, the first pillar is positioned under the laser. The laser power is increased to a preset value in less than a second, and Raman spectra are acquired in  $5 \text{ s}$  intervals, with each spectrum processed in real time to obtain temperature (from Si bands shifts) and CNT G- and D-band areas. Nanotube nucleation and growth are

detected by the appearance and increase in intensity of G- and D-bands seen at  $\sim 1590$  and  $\sim 1350$   $\text{cm}^{-1}$ . Upon experiment completion (300 s typical time), the next pillar is moved under the laser and the experimental cycle is repeated with a new growth recipe. This way, up to 25 experiments can be done in a fully automatic mode without human intervention.

Additional *ex situ* Raman characterization was done in Renishaw InVia Raman system with 532 nm excitation. The light collection efficiency and resolution in the commercial Raman system are notably better compared to that in the ARES spectrometer, in addition to much longer exposures afforded. This way, *ex situ* characterization helped to obtain Raman spectra with better signal-to-noise ratio. Electron microscopy characterization was done in FEI Sirion SEM equipped with field-emission gun, at 3–5 keV acceleration voltage to reduce charging.

Some experiments result in the growth of just one CNT, while others result in dozens of nanotubes scattered on the pillar surface, as seen in SEM images.

Logical regression analysis utilized Matlab R2012b statistics toolbox function "GeneralizedLinearModel.stepwise". The predictor variable matrix is constructed with  $\text{C}_2\text{H}_4$  partial pressure,  $\text{H}_2$  partial pressure,  $\text{H}_2\text{O}$  concentration, and temperature of each experiment. Two separate binomial response vectors,  $p_{\text{SWNT}}$  and  $p_{\text{MWNT}}$ , are constructed for SWNT and MWNT models: the first contains 1 when the experiment resulted in SWNT growth and 0 for outcomes with no SWNT (eq 2); the second contains 1 when the experiment resulted in MWNT growth and 0 for outcomes with no MWNT (eq 3). The outputs of the models are probabilities of the response,  $\chi_{\text{SWNT}}$  and  $\chi_{\text{MWNT}}$ , respectively, shown in eqs 2 and 3 for four actual experiments.

	Predictor variable matrix	response	output
experiment	$P(\text{C}_2\text{H}_4)$ $P(\text{H}_2)$ $T$ $\text{H}_2\text{O}$	$p_{\text{SWNT}}$	$\chi_{\text{SWNT}}$
1	—	—	1
2	—	—	0
3	—	—	1
4	—	—	0
..	—	—	..
.	—	—	.

(2)

	Predictor variable matrix	response	output
experiment	$P(\text{C}_2\text{H}_4)$ $P(\text{H}_2)$ $T$ $\text{H}_2\text{O}$	$p_{\text{MWNT}}$	$\chi_{\text{MWNT}}$
1	—	—	0
2	—	—	1
3	—	—	1
4	—	—	0
..	—	—	..
.	—	—	.

(3)

The predictor distribution is assumed normal and the response distribution binomial, with default logit link function.<sup>35</sup> Similar approaches are found in the literature when logical regression analysis is applied to the outcomes of medical trials, where discrete predictor variables might include gender,<sup>45</sup> race,<sup>45</sup> appearance of pain,<sup>44</sup> ulcer classification<sup>44</sup> and discrete responses might be healing,<sup>44</sup> appearance of certain symptoms,<sup>45</sup> etc.

The method begins with an initial model that includes all available predictor variables and their interactions; that is all linear and quadratic terms. Then at each step the method searches for terms to add or eliminate by comparing models with and without a potential term based on the *p*-value. The *p*-value is the probability of obtaining a test statistic result close to the one actually observed assuming that the null hypothesis is true.<sup>35</sup> The term is removed from the model if it fails statistical significance test, that is, *p* > 0.05,<sup>35</sup> and added or retained if significant. The sequence terminates when no single step improves the model.

All terms containing argon partial pressure and total pressure in the growth chamber were consistently eliminated as statistically insignificant, while terms containing temperature, water concentration, partial pressures of ethylene and hydrogen, and interactions thereof were found to be significant.

*Conflict of Interest:* The authors declare no competing financial interest.

*Acknowledgment.* The authors gratefully acknowledge funding from the Air Force Office of Scientific Research.

*Supporting Information Available:* Additional figures and experimental details. This material is available free of charge via the Internet at <http://pubs.acs.org>.

## REFERENCES AND NOTES

- Radushkevich, L. V.; Lukyanovich, V. M. On the Carbon Structure Formed during Thermal Decomposition of Carbon Monoxide in the Presence of Iron. *Zh. Fiz. Khim.* **1952**, *26*, 88–95(in Russian).
- Koyama, T.; Endo, M.; Onuma, Y. Carbon Fibers Obtained by Thermal Decomposition of Vaporized Hydrocarbon. *Jpn. J. Appl. Phys.* **1972**, *11*, 445–449.
- Baker, R. T. K.; Barber, M. A.; Harris, P. S.; Feates, F. S.; Waite, R. J. Nucleation and Growth of Carbon Deposits from the Nickel Catalyzed Decomposition of Acetylene. *J. Catal.* **1972**, *26*, 51–62.
- Oberlin, A.; Endo, M.; Koyama, T. Filamentous Growth of Carbon through Benzene Decomposition. *J. Cryst. Growth* **1976**, *32*, 335–349.
- Iijima, S.; Ichihashi, T. Single-Shell Carbon Nanotubes of 1-nm Diameter. *Nature* **1993**, *363*, 603–605.
- Bethune, D. S.; Kiang, C. H.; De Vries, M. S.; Gorman, G.; Savoy, R.; Vazquez, J.; Beyers, R. Cobalt-Catalysed Growth of Carbon Nanotubes with Single-Atomic-Layer Walls. *Nature* **1993**, *363*, 605–607.
- Dai, H.; Rinzler, A. G.; Nikolaev, P.; Thess, A.; Colbert, D. T.; Smalley, R. E. Single-Wall Nanotubes Produced by Metal-Catalyzed Disproportionation of Carbon Monoxide. *Chem. Phys. Lett.* **1996**, *260*, 471–475.
- Hafner, J. H.; Bronikowski, M. J.; Azamian, B. R.; Nikolaev, P.; Rinzler, A. G.; Colbert, D. T.; Smith, K. A.; Smalley, R. E. Catalytic Growth of Single-Wall Carbon Nanotubes from Metal Particles. *Chem. Phys. Lett.* **1998**, *296*, 195–202.
- Cheng, H. M.; Li, F.; Sun, X.; Brown, S. D. M.; Pimenta, M. A.; Marucci, A.; Dresselhaus, G.; Dresselhaus, M. S. Bulk Morphology and Diameter Distribution of Single-Walled Carbon Nanotubes Synthesized by Catalytic Decomposition of Hydrocarbons. *Chem. Phys. Lett.* **1998**, *289*, 602–610.
- Satishkumar, B. C.; Govindaraj, A.; Sen, R.; Rao, C. N. R. Single-Walled Nanotubes by the Pyrolysis of Acetylene–Organometallic Mixtures. *Chem. Phys. Lett.* **1998**, *293*, 47–52.
- Nikolaev, P.; Bronikowski, M. J.; Bradley, R. K.; Rohmund, F.; Colbert, D. T.; Smith, K. A.; Smalley, R. E. Gas-Phase Catalytic Growth of Single-Walled Carbon Nanotubes from Carbon Monoxide. *Chem. Phys. Lett.* **1999**, *313*, 91–97.
- Hata, K.; Futaba, D. N.; Mizuno, K.; Namai, T.; Yumura, M.; Iijima, S. Water-Assisted Highly Efficient Synthesis of Impurity-Free Single-Walled Carbon Nanotubes. *Science* **2004**, *306*, 1362–1364.
- Yasuda, S.; Futaba, D. N.; Yumura, M.; Iijima, S.; Hata, K. Diagnostics and Growth Control of Single-Walled Carbon Nanotube Forests Using a Telecentric Optical System for *In Situ* Height Monitoring. *Appl. Phys. Lett.* **2008**, *93*, 143115–1–143115–3.
- Chakrabarti, S.; Nagasaka, T.; Yoshikawa, Y.; Pan, L.; Nakayama, Y. Growth of Super Long Aligned Brush-like Carbon Nanotubes. *Jpn. J. Appl. Phys.* **2006**, *45*, L720–L722.
- Ci, L.; Vajtai, R.; Ajayan, P. M. Vertically Aligned Large-Diameter Double-Walled Carbon Nanotube Arrays Having Ultralow Density. *J. Phys. Chem. C* **2007**, *111*, 9077–9080.
- Yamada, T.; Namai, T.; Hata, K.; Futaba, D. N.; Mizuno, K.; Fan, J.; Yudasaka, M.; Yumura, M.; Iijima, S. Size-Selective Growth of Double-Walled Carbon Nanotube Forests from Engineered Iron Catalysts. *Nat. Nanotechnol.* **2006**, *1*, 131–136.
- Zhu, L.; Xiu, Y.; Hess, D. W.; Wong, C. P. Aligned Carbon Nanotube Stacks by Water-Assisted Selective Etching. *Nano Lett.* **2005**, *5*, 2641–2645.
- Patole, S. P.; Alegaonkar, P. S.; Shin, H. C.; Yoo, J. B. Alignment and Wall Control of Ultra Long Carbon Nanotubes in Water Assisted Chemical Vapour Deposition. *J. Phys. D: Appl. Phys.* **2008**, *41*, 155311–1–155311–6.

19. Zhao, B.; Futaba, D. N.; Yasuda, S.; Akoshima, M.; Yamada, T.; Hata, K. Exploring Advantages of Diverse Carbon Nanotube Forests with Tailored Structures Synthesized by Supergrowth from Engineered Catalysts. *ACS Nano* **2009**, *3*, 108–114.
20. Noda, S.; Hasegawa, K.; Sugime, H.; Kakehi, K.; Zhang, Z. Y.; Maruyama, S.; Yamaguchi, Y. Millimeter-Thick Single-Walled Carbon Nanotube Forests: Hidden Role of Catalyst Support. *Jpn. J. Appl. Phys.* **2007**, *46*, L399–L401.
21. Puretzky, A. A.; Geohegan, D. B.; Jesse, S.; Ivanov, I. N.; Eres, G. *In Situ* Measurements and Modeling of Carbon Nanotube Array Growth Kinetics during Chemical Vapor Deposition. *Appl. Phys. A: Mater. Sci. Process.* **2005**, *81*, 223–240.
22. Wood, R. F.; Pannala, S.; Wells, J. C.; Puretzky, A. A.; Geohegan, D. B. Simple Model of the Interrelation between Single- and Multiwall Carbon Nanotube Growth Rates for the CVD Process. *Phys. Rev. B* **2007**, *75*, 235446-1–235446-8.
23. Wirth, C. T.; Zhang, C.; Zhong, G.; Hofmann, S.; Robertson, J. Diffusion- and Reaction-Limited Growth of Carbon Nanotube Forests. *ACS Nano* **2009**, *3*, 3560–3566.
24. Rao, R.; Liptak, D.; Cherukuri, T.; Yakobson, B. I.; Maruyama, B. *In Situ* Evidence for Chirality-Dependent Growth Rates of Individual Carbon Nanotubes. *Nat. Mater.* **2012**, *11*, 213–216.
25. Rao, R.; Pierce, N.; Liptak, D.; Hooper, D.; Sargent, G.; Semiatin, S. L.; Curtarolo, S.; Harutyunyan, A.; Maruyama, B. Revealing the Impact of Catalyst Phase Transition on Carbon Nanotube Growth by *In Situ* Raman Spectroscopy. *ACS Nano* **2013**, *7*, 1100–1107.
26. Moisala, A.; Nasibulin, A. G.; Kauppinen, E. I. The Role of Metal Nanoparticles in the Catalytic Production of Single-Walled Carbon Nanotubes—A Review. *J. Phys.: Condens. Matter* **2003**, *15*, S3011–S3036.
27. Chan, E. M.; Xu, C.; Mao, A. W.; Han, G.; Owen, J. S.; Cohen, B. E.; Milliron, D. J. Reproducible, High-Throughput Synthesis of Colloidal Nanocrystals for Optimization in Multi-dimensional Parameter Space. *Nano Lett.* **2010**, *10*, 1874–1885.
28. King, R. D.; Rowland, J.; Oliver, S. J.; Young, M.; Aubrey, W.; Byrne, E.; Liakata, M.; Markham, M.; Pir, P.; Soldatova, L. N.; et al. The Automation of Science. *Science* **2009**, *324*, 85–89.
29. Sparkes, A.; Aubrey, W.; Byrne, E.; Clare, A.; Khan, M. N.; Liakata, M.; Markham, M.; Rowland, J.; Soldatova, L. N.; Whelan, K. E.; et al. Towards Robot Scientists for Autonomous Scientific Discovery. *Autom. Exp.* **2010**, *2*, 1-1–1-11.
30. Bilsland, E.; Sparkes, A.; Williams, K.; Moss, H. J.; de Clare, M.; Pir, P.; Rowland, J.; Aubrey, W.; Pateman, R.; Young, M.; et al. Yeast-Based Automated High-Throughput Screens To Identify Anti-parasitic Lead Compounds. *Open Biol.* **2013**, *3*, 120158-1–120158-13.
31. Cassell, A. M.; Verma, S.; Delzeit, L.; Meyyappan, M.; Han, J. Combinatorial Optimization of Heterogeneous Catalysts Used in the Growth of Carbon Nanotubes. *Langmuir* **2001**, *17*, 260–264.
32. Ng, H. T.; Chen, B.; Koehne, J. E.; Cassell, A. M.; Li, J.; Han, J.; Meyyappan, M. Growth of Carbon Nanotubes: A Combinatorial Method To Study the Effects of Catalysts and Underlayers. *J. Phys. Chem. B* **2003**, *107*, 8484–8489.
33. Noda, S.; Tsuji, Y.; Murakami, Y.; Maruyama, S. Combinatorial Method To Prepare Metal Nanoparticles That Catalyze the Growth of Single-Walled Carbon Nanotubes. *Appl. Phys. Lett.* **2005**, *86*, 173106-1–173106-3.
34. Balkanski, M.; Wallis, R. F.; Haro, E. Anharmonic Effects in Light Scattering Due to Optical Phonons in Silicon. *Phys. Rev. B* **1983**, *28*, 1928–1934.
35. Agresti, A. *Categorical Data Analysis*, 3<sup>rd</sup> ed.; John Wiley & Sons, Inc.: Hoboken, NJ, 2013; Chapter 5.
36. Amama, P. B.; Pint, C. L.; McJilton, L.; Kim, S. M.; Stach, E. A.; Murray, P. T.; Hauge, R. H.; Maruyama, B. Role of Water in Super Growth of Single-Walled Carbon Nanotube Carpets. *Nano Lett.* **2009**, *9*, 44–49.
37. Kim, S. M.; Pint, C. L.; Amama, P. B.; Zakharov, D. N.; Hauge, R. H.; Maruyama, B.; Stach, E. A. Evolution in Catalyst Morphology Leads to Carbon Nanotube Growth Termination. *J. Phys. Chem. Lett.* **2010**, *1*, 918–922.
38. Patole, S. P.; Alegaonkar, P. S.; Lee, H. C.; Yoo, J. B. Optimization of Water Assisted Chemical Vapor Deposition Parameters for Super Growth of Carbon Nanotubes. *Carbon* **2008**, *46*, 1987–1993.
39. Futaba, D. N.; Hata, K.; Yamada, T.; Mizuno, K.; Yumura, M.; Iijima, S. Kinetics of Water-Assisted Single-Walled Carbon Nanotube Synthesis Revealed by a Time-Evolution Analysis. *Phys. Rev. Lett.* **2005**, *95*, 056104-1–056104-4.
40. Cortes, C.; Vapnik, V. N. Support-Vector Networks. *Mach. Learn.* **1995**, *20*, 273–297.
41. Breiman, L. Random Forests. *Mach. Learn.* **2001**, *45*, 5–32.
42. Powell, W. B.; Ryzhov, I. O. *Optimal Learning*; John Wiley & Sons, Inc.: Hoboken, NJ, 2012; Chapter 5.
43. Poleski, J.; Krein, M.; Barto, R. Learning from an Informatics Approach Applied to Materials Design. *Nanotech. Conf. Expo 2013* **2013**, *2*, 642–645.
44. Massarrat, S.; Muller, H. G.; Schmitz-Moormann, P. Risk Factors for Healing of Duodenal Ulcer under Antacid Treatment: Do Ulcer Patients Need Individual Treatment? *Gut* **1988**, *29*, 291–297.
45. Cinkotai, F. F.; Rigby, A.; Pickering, C. A. C.; Seaborn, D.; Faragher, E. Recent Trends in the Prevalence of Byssinotic Symptoms in the Lancashire Textile Industry. *Br. J. Ind. Med.* **1988**, *45*, 782–789.
46. Oliver, C. R.; Westrick, W.; Koehler, J.; Brieland-Shoultz, A.; Anagnostopoulos-Politis, I.; Cruz-Gonzalez, T.; Hart, A. J. Robofurnace: A Semi-Automated Laboratory Chemical Vapor Deposition System for High-Throughput Nanomaterial Synthesis and Process Discovery. *Rev. Sci. Instrum.* **2013**, *84*, 115105-1–115105-14.